Journal of Materials Chemistry A

ROYAL SOCIETY OF CHEMISTRY

PAPER

View Article Online
View Journal | View Issue

Cite this: J. Mater. Chem. A, 2026, 14, 1063

X-ray imaging with AI-driven super-resolution deep learning for investigating battery electrode microstructural properties over cycling

Mohammad Javad Shojaei,[a] Guanting Li,[a] Aditya Ramadas[a] and Chun Huang *[abc]

Rechargeable batteries are promising for transition to clean energy. This study investigates microstructural dynamics of $LiNi_{0.8}Mn_{0.1}Co_{0.1}O_2$ (NMC811)-based cathodes over cycling using X-ray computed tomography (XCT). There is a long-standing imaging challenge of compromising between the large field-of-view (FoV) to be representative of the electrodes and high resolution to observe fine details of individual particles. Here, we provide a framework that mitigates this trade-off by comparing two deep learning models—convolutional neural networks (CNNs) and generative adversarial networks (GANs)—for super-resolution enhancement of the XCT data to achieve both a large FoV (4 times larger) and sub-micron resolution. We fabricated NMC811 cathodes containing different initial porosities (0.46–0.85) and tortuosities (1.24–2.74) by two different methods, directional ice templating (DIT) and dry processing to eliminate toxic organic solvents during fabrication. Micro-cracks inside individual NMC811 secondary particles and shifts in pixel intensity distributions were observed after 100 (dis)charge cycles. The DIT cathode exhibited larger irreversible volume expansion due to the more favorable ion diffusion kinetics and higher active material utilization. Interestingly, the higher pore volume and carbon binder domain (CBD) surrounding the NMC811 particles effectively accommodated the volume expansion, and the DIT cathode exhibited higher capacity retention over cycling than the dry coated cathode that exhibited initial lower porosity and higher tortuosity. A linear regression model was used to determine the correlation among the various microstructural properties such as porosity and tortuosity in the pristine state, and expansion after cycling to develop a framework for predicting the optimal initial microstructure and electrochemical performance over cycling.

Received 30th June 2025
Accepted 3rd November 2025

DOI: 10.1039/d5ta05257b

rsc.li/materials-a

[a]Department of Materials, Imperial College London, London, UK. E-mail: a.huang@imperial.ac.uk
[b]The Faraday Institution, Didcot, OX11 0RA, UK
[c]Research Complex at Harwell, Rutherford Appleton Laboratory, Didcot, OX11 0FA, UK

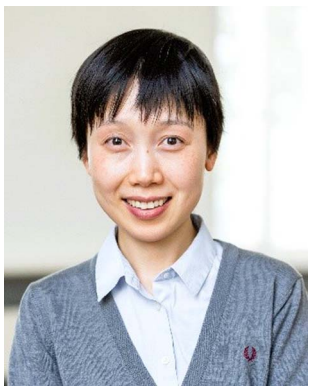

Chun Huang

Chun Huang is an Associate Professor of Energy Storage Materials at the Department of Materials, Imperial College London, United Kingdom. She obtained her undergraduate degree in Materials Science and Engineering (First Class Honours) at Imperial College London and PhD degree in Materials Science at the University of Oxford. She was awarded the EPSRC Open Fellowship, European Research Council (ERC) Starting Grant, and the Faraday Institution Industry Fellowship. She is a Co-Investigator of the Faraday Institution "Battery degradation – extending battery life" and "Nextrode – electrode manufacturing" programmes. Her research focuses on developing new materials, processing, and correlative imaging for electrochemical energy storage applications.

Introduction

Over the past decade, batteries have played a crucial role in the global effort to achieve zero emissions and enable the transition from fossil fuels to renewable energy sources.[1,2] Batteries have facilitated the widespread adoption of electric transportation and grid storage of intermittent renewable energy.[3] To meet diverse energy storage needs, a range of battery types have been developed.[4,5] For lithium-ion batteries, the $LiNi_{0.8}Mn_{0.1}Co_{0.1}O_2$ (NMC811) cathode material has gained significant interest due to its balance between energy density, power output, longevity, and thermal stability.[6,7]

Understanding how NMC811 behaves over cycling is essential for optimizing battery performance and longevity. At the crystal lattice scale, cycling-induced mechanical degradation is caused by anisotropic lattice expansion of NMC811 during lithium insertion.[8] Over the course of cycling, NMC811 undergoes microstructural changes that can impact the integrity and efficiency of the electrodes.[9,10] Crack formation is an important degradation mechanism that reduces battery performance. Recent electrochemical-mechanical modelling results show that during delithiation, although the primary NMC811 particles shrink, a volumetric expansion of the secondary particles occurs because of cracking due to the strain anisotropy of the primary particles.[11] The incompatible deformation from grain to grain induces large self-stresses that lead to cracks/fracture inside secondary particles and larger cracks between the secondary particles in the electrode microstructure.[12]

Our group has developed two sustainable methodologies for making electrodes with different microstructures: directional ice templating (DIT) for making electrodes with vertical pore arrays to improve the ion diffusion kinetics[13–15] and dry processing for making electrodes that eliminate toxic and combustible organic solvent *N*-methyl-2-pyrrolidone (NMP). The DIT electrode improves active material utilization in energy storage, but in turn the active material particles may exhibit larger volume changes over lithiation and delithiation.[12] On the other hand, the dry coated electrodes are more compact with higher pore tortuosity, but the compact microstructure may cause more strain during active material expansion, leading to cracks and reducing NMC811 capacity dramatically from ~190 mA h g^{-1} to <60 mA h g^{-1} over 80 cycles at a slow C/3 rate.[12,16]

To quantify spatially-resolved microstructural changes during cycling, X-ray computed tomography (XCT) imaging, neutron imaging, white light interferometry, *etc.* have been used.[17,18] XCT has emerged as a powerful technique widely used to visualize internal microstructures.[19–26] XCT reveals material degradation mechanisms, structural and phase changes, *etc.*, that affect battery performance and longevity.[19–21] One key challenge in XCT is the inherent trade-off between resolution and the field-of-view (FoV).[20,27] High-resolution imaging is necessary for capturing fine structural details but often focuses on a small area of the electrode that may not be completely representative of the sample. Conversely, imaging larger areas provides a broader FoV, but sacrifices resolution, making it difficult to discern finer details. Experimental methods have reached physical resolution limitations of existing XCT instruments.[28]

Deep learning models can improve image resolutions, *e.g.*, convolutional neural networks (CNNs) rely on a feature-based approach to learn the mapping between low- and high-resolution data, focusing on enhancing structural fidelity,[29,30] and generative adversarial networks (GANs) incorporate an adversarial component, where a generator produces high-resolution images and a discriminator evaluates their quality, often resulting in superior perceptual quality.[31,32] However, they have not been investigated in detail for XCT of different electrode microstructures for batteries. Furthermore, electrode microstructures include multiple properties such as porosity, pore tortuosity, particle volume changes, *etc.*; quantification and finding a relationship among these interlinked parameters is critical for optimising the electrode microstructure and minimising degradation, but it is challenging to find the complex relationship among the multiple property metrics using conventional methods.[19–21]

Here, we fabricate NMC811-based cathodes by both DIT and dry processing methodologies with different microstructural characteristics. We employ XCT imaging to observe and quantify NMC811-based electrode microstructural changes over 100 charge–discharge cycles. By monitoring critical microstructural parameters, we gain valuable insights into the extent of active material particle volume expansion, cracking, and its subsequent impact on battery degradation. We employ both deep learning approaches of CNNs and GANs to transform low-resolution, large FoV XCT data of the NMC811 electrodes into high-resolution, large FoV images to mitigate the main resolution–FoV trade-off challenge of imaging. We then employ a linear regression model to quantify and find the complex relationship among the different microstructural properties such as pristine porosity and tortuosity and volume expansion after cycling in order to guide the initial optimal microstructure design to minimise degradation over battery cycling. These advancements significantly enhance the capability of XCT imaging and analysis in battery research, providing deeper insights into material behaviour and degradation mechanisms.

Results and discussion

Machine learning procedures

Each solid free-standing NMC811 cathode was scanned twice, one at a low resolution of 2.3 μm per pixel and the other at a higher resolution of 0.74 μm per pixel. The resolution was adjusted by modifying the distance between the X-ray source and the electrode, with the closer proximity enabling a higher resolution scan.

To prepare the data for training the super-resolution models, we extracted 128 × 128 pixel sub-samples from 3D XCT image stacks. The data consisted of paired low-resolution (input) and high-resolution (ground truth) images that were pre-registered and scaled to ensure identical dimensions, enabling direct comparison (Fig. 1). A total of 182 976 sub-samples were extracted, with each patch measuring 128 × 128 pixels. The

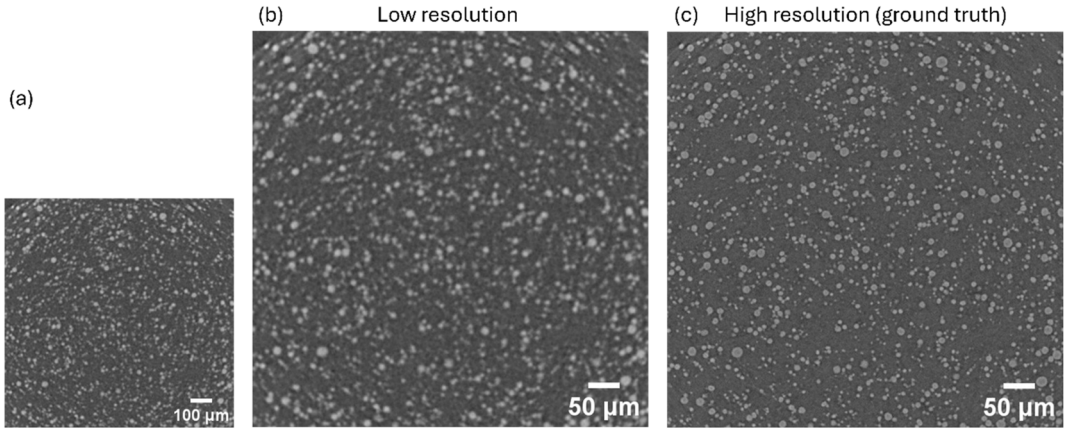

Fig. 1 (a) Example of experimental low-resolution image of the NMC811 cathode acquired at 2.3 µm per pixel, (b) corresponding scaled-up version of the low-resolution image, and (c) experimental high-resolution image obtained at 0.74 µm per pixel.

resulting datasets had dimensions of (182 976, 128, 128) for both the low-resolution and high-resolution data. This approach enabled efficient preparation of a large number of image patches, providing a comprehensive dataset to train deep learning models for the super-resolution tasks.

The CNN architecture employed in this study is based on the Super-Resolution Convolutional Neural Network (SRCNN) framework, which has been used in image super-resolution tasks.[33–36] To further improve the quality of low-resolution images through pixel-wise refinement, we enhanced the standard SRCNN by incorporating residual connections and additional convolutional layers for more effective feature extraction. The architecture, depicted in Fig. 2, illustrates how the convolutional and residual layers work together to enhance image resolution.

The proposed deep learning model is designed for super-resolution of grayscale images with dimensions of 128 × 128. The network architecture is an enhanced SRCNN with residual blocks to improve training stability and feature learning. The model input is a single-channel image, and the output is a reconstructed image of the same size. The network begins with an initial convolutional layer containing 64 filters of size 9 × 9 and ReLU activation, which extracts low-level features from the input image. This is followed by three residual blocks, each consisting of two 3 × 3 convolutional layers with ReLU activation and skip connections to preserve the input signal and mitigate vanishing gradient issues. After the residual blocks, an additional convolutional layer with 32 filters of size 5 × 5 and ReLU activation further refines the features. A final convolutional layer with a single 5 × 5 filter and linear activation reconstructs the output image. The network also effectively balances computational efficiency and reconstruction quality, making it well-suited for super-resolution tasks.

The GAN model developed for super-resolution of XCT images consists of two key components: the generator and the discriminator. The generator is responsible for transforming low-resolution images into high-resolution outputs, while the discriminator assesses the quality of the generated images by distinguishing between real and fake (generated) samples. As shown in Fig. 3, the architecture of the generator is designed for image resolution enhancement, with the discriminator following a similar structure.

The generator follows a fully convolutional design tailored for 128 × 128 grayscale low-resolution input images. It begins with a convolutional layer of 64 filters using a kernel size of (3, 3), ReLU activation, and the 'same' padding to retain the spatial dimensions. This is followed by a second convolutional layer with 128 filters and ReLU activation, also using the 'same' padding. Finally, a third convolutional layer with a single filter (1 channel) and linear activation produces the high-resolution output, preserving the real-valued nature of the image. The generator is trained to learn a pixel-to-pixel mapping from low-resolution to high-resolution images. The discriminator is designed to assess the authenticity of images. It accepts 128 × 128 grayscale images and starts with a convolutional layer of 64 filters (3 × 3 kernel, ReLU activation, 'same' padding), followed by a MaxPooling layer to reduce the spatial dimensions. A second convolutional layer with 128 filters and ReLU activation is applied before flattening the feature maps. The final layer is a single-node dense layer with linear activation that outputs a continuous scalar value representing the "realness" of the

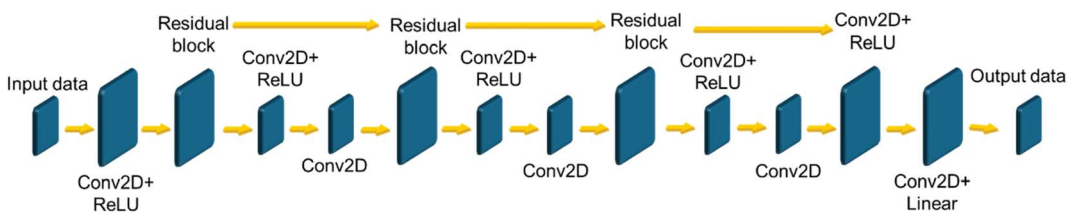

Fig. 2 Architecture of the SRCNN model utilized in this study, illustrating the convolutional and residual layers.

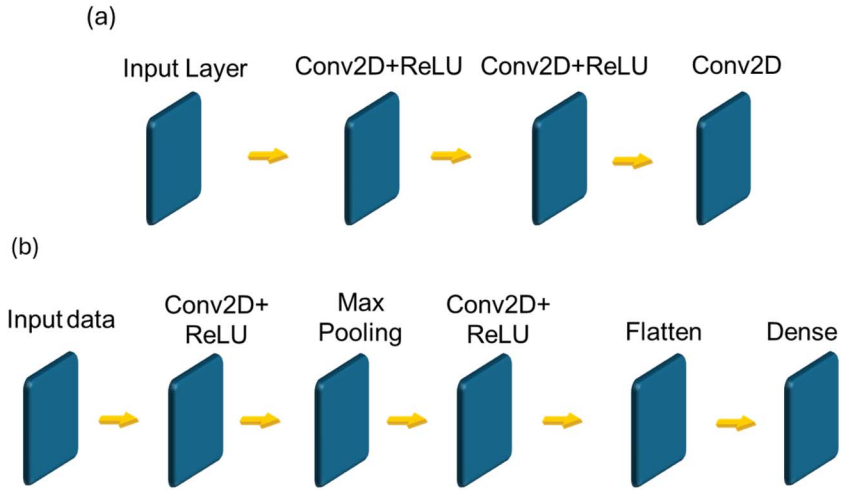

Fig. 3 The GAN model architecture used for image resolution enhancement: illustration of (a) the generator and (b) the discriminator components.

input image. The discriminator is trained to distinguish between real high-resolution images and generator outputs. During generator training, the discriminator weights are frozen to ensure that only the generator is updated. The combination of architectural design, adversarial training, evaluation with multiple quantitative metrics, and qualitative analysis ensures a comprehensive assessment of the ability of the models to generate high-quality high-resolution images suitable for downstream tasks such as segmentation.

For training both models, the dataset is split into 80% for training and 20% for validation. The images are normalized to the range [0, 1] to facilitate faster convergence. Both models were trained using the Adam optimizer with a learning rate of 0.0001, a batch size of 32, and for 28 epochs, containing approximately one million trainable parameters. To improve training efficiency and prevent overfitting, callbacks are used, including a learning rate scheduler that reduces the learning rate when validation loss plateaus are reached and a model checkpoint to save the best-performing model based on validation loss. Performance of the model is evaluated using pixel-wise metrics such as mean squared error (MSE) as the primary loss function and mean absolute error (MAE) as an additional metric. Another two quantitative metrics used are structural similarity index measure (SSIM) and peak signal-to-noise ratio (PSNR).[37–39] SSIM is a perceptual metric that assesses similarity between generated and ground truth images, considering luminance, contrast, and structural information. A higher SSIM indicates that the generated image preserves important structural details of the high-resolution reference. PSNR measures the ratio between the maximum pixel intensity and the reconstruction error; higher PSNR values indicate better fidelity to the original image. In addition to these metrics, a qualitative comparison is performed by analyzing histogram distributions of pixel intensities in both the original high-resolution images and the generated outputs. Training of both models also incorporates random mini-batch sampling to improve generalization. During each epoch, the training and validation metrics are tracked and saved. The model that performs best on the validation set is retained for future use.

While both the CNN and GAN models demonstrate strong performance in super-resolution tasks, certain limitations should be considered. Although the models are trained on 128 $\times$ 128 sub-samples extracted from larger images, reconstructing the full-size images from these patches may occasionally introduce boundary artifacts. The CNN model is designed for single-channel grayscale images, and while highly effective for the current dataset, extending it to multi-channel or colour images may require additional adaptation.[40,41] To prevent overfitting and underfitting, both models incorporate validation-based monitoring, early stopping, learning rate scheduling, and mini-batch training, ensuring stable and generalized performance.[42–44] Adversarial training introduces inherent challenges such as careful tuning of hyperparameters, but it also enables the GAN model to learn richer representations compared to standard CNNs.[45] Finally, as with all data-driven models, performance depends on the diversity and quality of the training dataset. Despite these considerations, both models provide reliable and robust super-resolution results, significantly enhancing image quality and structural details, and offering a strong foundation for future improvements and applications.

Evaluation of CNN and GAN models for super-resolution performance

We observed distinct learning behaviour between the GAN and CNN models, as depicted in Fig. 4. The GAN model (Fig. 4a and b) demonstrated a rapid decline in both training and validation errors, stabilizing around epoch 10. The MSE and MAE values plateaued at approximately 0.015 and 0.05, respectively. This indicates an efficient early learning phase, suggesting that the GAN architecture quickly captures the essential features for super-resolution tasks. The CNN model (Fig. 4c and d) demonstrated a sharp decrease in both MSE and MAE even earlier at around epoch 8. The training MSE for the CNN model

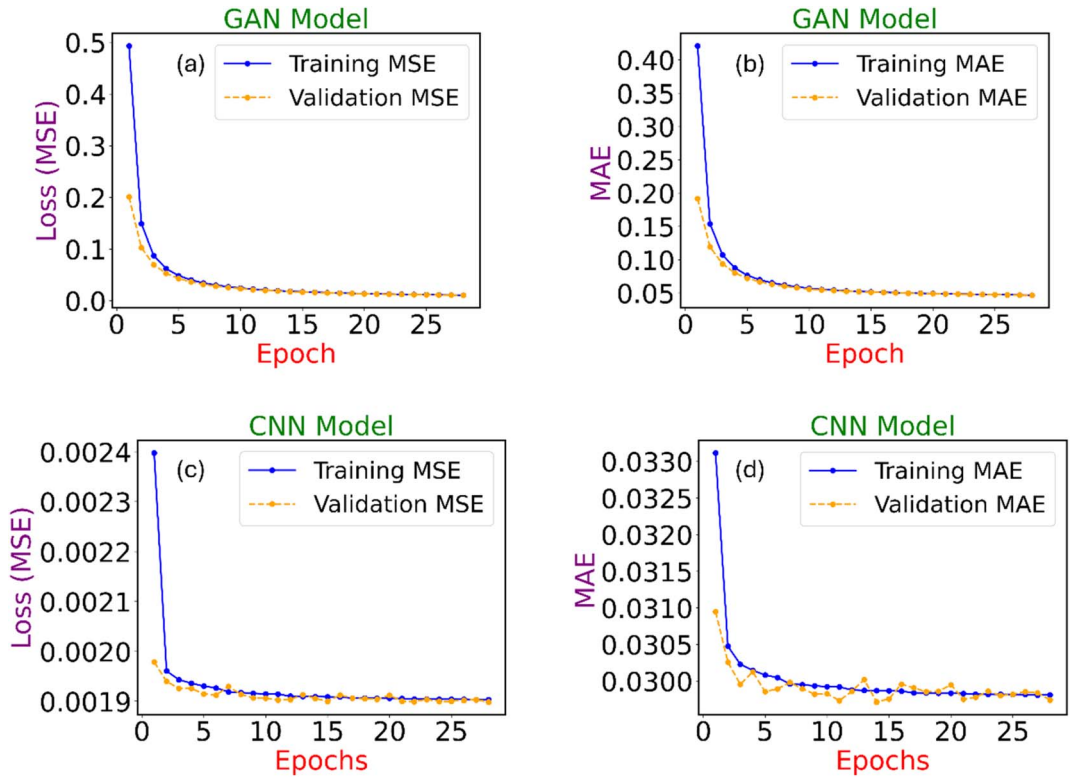

Fig. 4 (a) Mean squared error (MSE); and (b) mean absolute error (MAE) *versus* epochs for both the training and validation datasets for the GAN model. (c) MSE; and (d) MAE *versus* epochs for the CNN model.

settled at a lower value of approximately 0.0019, with the validation MSE following closely, indicating robust learning with minimal overfitting. Similarly, the training MAE stabilized at about 0.03. The CNN model achieved an MSE reduction of nearly 90% compared to the GAN model, and its MAE was ~40% lower. Therefore, the CNN model provides higher accuracy compared to the GAN model for image super-resolution in this application.

The experimental low-resolution XCT image of a fabricated NMC811 electrode (Fig. 5a) was transformed into high-resolution images with the same FoV (554 μm × 554 μm) using the GAN model (Fig. 5b) and the CNN model (Fig. 5c). To facilitate visual comparison, Fig. 5d–f presents the images of the same FoV covering the electrode sample of 1 mm in diameter (images of 554 μm × 554 μm) but cropped to allow easier comparison of the fine details in the images. The term zoomed-in does not indicate optical magnification but rather refers to the cropped region in the yellow box in Fig. 5c. The images show that the CNN model preserves finer details and more accurately maintains the integrity of individual particles (blue boxes in Fig. 5d–f). In contrast, the GAN model tends to merge some of the NMC particles that were separate in the ground truth image, whereas the CNN model successfully resolves them.

Fig. 5g and h presents normalized histograms of intensity distributions for low-resolution images (red), ground truth images (green), and model predictions (blue) from both the GAN and CNN models. In both plots, the low-resolution images display a narrower intensity distribution, with most values concentrated around lower intensity levels. The ground truth images, on the other hand, exhibit a broader intensity range, reflecting higher quality and more detailed information. Both the GAN and CNN models shifted the intensity distribution of the low-resolution images toward that of the ground truth. The results confirmed the CNN model shows a broader range and closer alignment with the ground truth distribution than the GAN model.

Table 1 shows the calculated SSIM and PSNR for the GAN- and CNN-generated images compared with the experimental high-resolution ground truth image, where SSIM indicates how similar two images are by focusing on their structure, brightness, and contrast; and PSNR shows how much noise is in the image compared to the original, with higher values meaning that the image is closer to the ground truth for both SSIM and PSNR. The "No Model" scenario, which directly compares experimental low-resolution images with experimental high-resolution ground truth, shows the lowest performance, with an SSIM of 0.66 and a PSNR of 22.15. These values highlight the significant disparity in quality between the low- and high-resolution images of the same electrode region. The GAN model achieved an SSIM of 0.82 and a PSNR of 26.45. The CNN model outperformed the GAN, achieving an SSIM of 0.92 and a PSNR of 30.12, again confirming that the CNN model excels in preserving fine details and reducing noise, making it more effective for high-resolution image reconstruction.

To further assess the performance of the GAN and CNN models in enhancing image resolution, we analyzed the particle

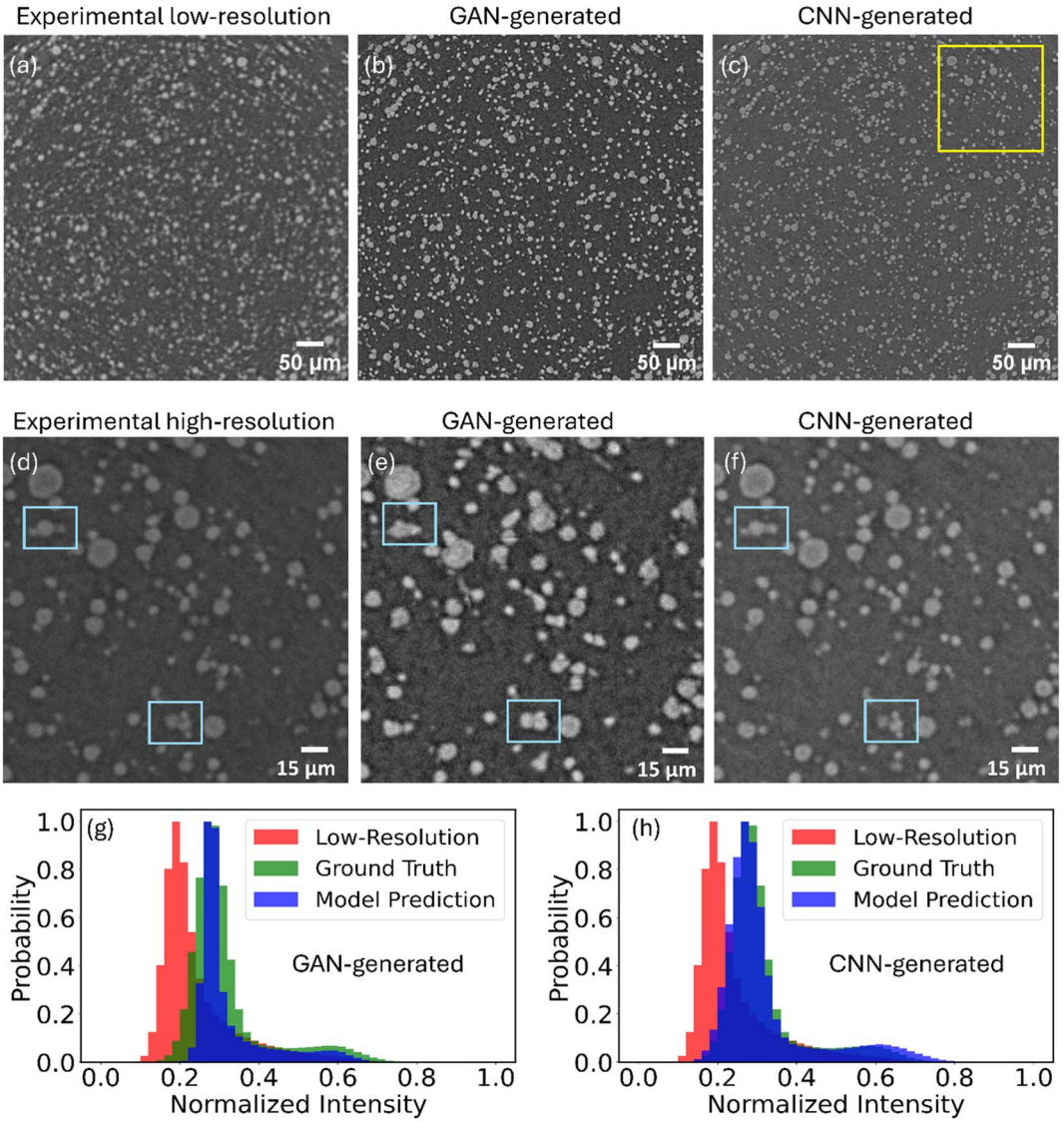

Fig. 5 (a) Experimental low-resolution image. (b) GAN model-generated; and (c) CNN model-generated high-resolution images. The yellow square in (c) shows the position of the zoomed-in section in (d–f). Cropped section to show the zoomed-in section of (d) experimental high-resolution image (ground truth), (e) GAN model-generated, and (f) CNN model-generated high-resolution images. The term zoomed-in does not indicate optical magnification but rather refers to the cropped region (highlighted by the yellow box in Fig. 5c) to allow easier comparison of the fine details in the images. The blue rectangles in (d–f) indicate the same regions for better comparison. Normalized histograms of intensity distributions for experimental low-resolution, experimental high-resolution (ground truth), and predicted images by (g) GAN and (h) CNN.

Table 1 Quantitative comparison of the performance of the GAN and CNN models using SSIM and PSNR

Model	SSIM	PSNR
No model (experimental low-resolution)	0.66	22.15
GAN	0.82	26.45
CNN	0.92	30.12

sizes, porosity, and tortuosity from matched regions of interest (ROIs) in different datasets. To avoid potential data leakage due to correlations between patches from the same 3D scan, all reported results (SSIM, PSNR, and microstructural parameters including particle sizes, porosity, and tortuosity) were evaluated on fully unseen datasets at the sample level. No patches from the same electrode were used during training or testing. Fig. 6 compares the particle sizes extracted from the original high-resolution and low-resolution images with those obtained from the super-resolved images generated by the CNN and GAN models from the low-resolution input. The low-resolution image (Fig. 6b) shows a noticeably shifted and a wider particle size distribution compared to that of the high-resolution reference (Fig. 6a), indicating loss of fine structural details in the low-resolution data. Both the super-resolution models improved the particle size representation, but the CNN-generated image (Fig. 6c) more closely matches the high-resolution distribution, capturing the peak and spread of particle diameters with higher accuracy. The GAN-generated image (Fig. 6d)

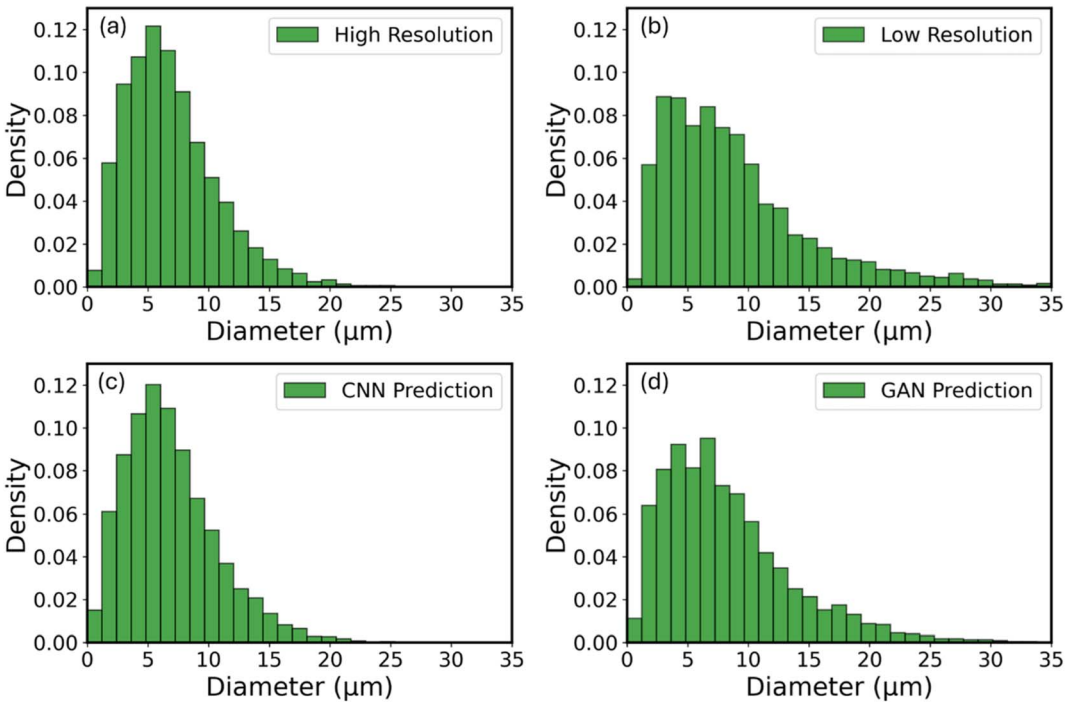

Fig. 6 Particle sizes for different datasets: (a) original experimental high-resolution image, (b) original experimental low-resolution image, (c) CNN super-resolved image, and (d) GAN super-resolved image; (c) and (d) were generated from the low-resolution image.

also improves over the low-resolution data, but the distribution shows a slight deviation from the high-resolution reference.

To further assess metric-level validation on matched ROIs, Fig. 7 presents a comparison of porosity and tortuosity derived from high-resolution and low-resolution electrode scans and CNN super-resolved and GAN super-resolved images. The bar plots show mean values calculated across multiple ROIs, with error bars indicating the standard deviation, highlighting the variability within each dataset.

Fig. 7 shows that porosity and tortuosity values derived from the CNN super-resolved images closely align with those obtained from the high-resolution dataset both in terms of mean values and variability across different ROIs, further supporting the superior performance of the CNN model in preserving structural features. The GAN-generated metrics show slightly larger deviations, particularly in tortuosity. The error bars, representing standard deviations across ROIs, also indicate that the CNN model maintains consistency in structural quantification, reinforcing its reliability for downstream analysis. Future work could extend to the incorporation of nano-CT or FIB-SEM on selected ROIs.

Given the superior preservation of particle details by the CNN model, we applied the best-trained CNN to unseen experimental XCT images of NMC811 cathodes acquired at low resolution but with a larger FoV covering an electrode sample of 2 mm in diameter. The experimental low-resolution image (Fig. 8a) reveals limited particle-level details due to physical resolution constraints. Achieving high-resolution imaging typically requires placing the sample closer to the X-ray source, which inherently reduces the FoV and makes it impractical to scan large samples. By applying our best-trained CNN model to the low-resolution image of this larger sample, we were able to reconstruct high-

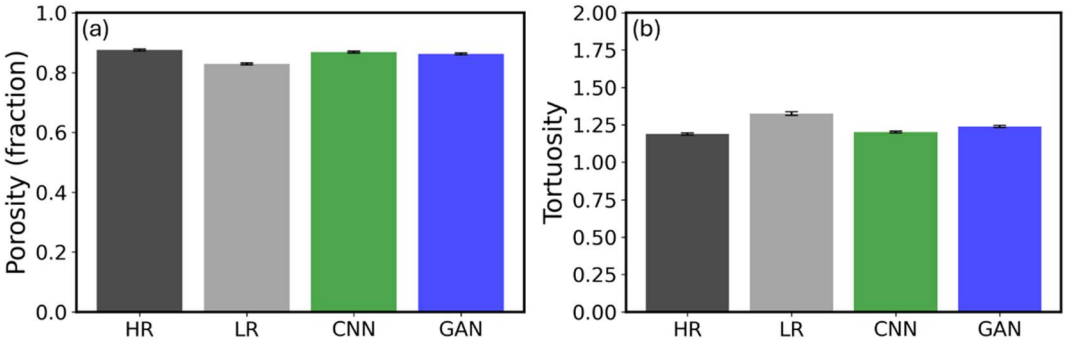

Fig. 7 Comparison of (a) porosity and (b) tortuosity for matched ROIs in different datasets: high-resolution (HR), low-resolution (LR), CNN super-resolved, and GAN super-resolved images. Bars represent the mean values across different ROIs, and error bars indicate the standard deviation.

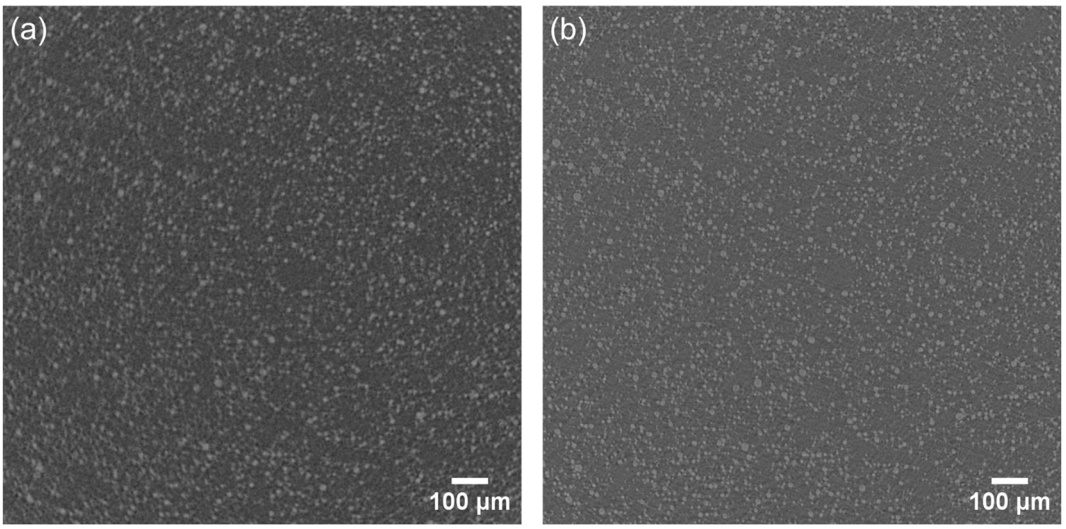

Fig. 8 (a) Experimental low-resolution: the large field of view (FoV) unseen image of the NMC811 cathode. (b) Enhanced resolution: the large FoV image generated by using the trained CNN model, improving the level of detail of particle and microstructural characteristics.

quality features that preserve particle boundaries, reduce noise, and enhance structural clarity of the same large FoV covering the electrode sample of 2 mm in diameter (Fig. 8b). This demonstrates that our deep learning approach can effectively generate high-resolution representations while increasing the FoV by 4 times (compared with the same experimentally achievable high-resolution images), even when direct experimental high-resolution imaging is not feasible due to hardware limitations. This approach mitigates the conventional resolution–FoV trade-off and enabling detailed analysis of large-scale samples without compromising resolution. Separately, the workflow could also be applied to accelerate scanning by acquiring low-resolution images and enhancing them to high resolution using a trained model, thereby reducing total scan time. While this time-saving application was not implemented here, approximate timings indicate that acquiring a high-resolution scan (0.74 μm voxel size) using the Micro XCT scanner settings takes ~3.5 hours, a low-resolution scan (2.3 μm voxel size) takes ~45 minutes, and applying the trained CNN to enhance resolution requires ≤10 minutes per volume. The one-off setup, including paired ROI acquisition, registration, curation, and model training, represents the initial effort. These numbers suggest that, for similar electrodes, super-resolution could substantially reduce scan time. We also plan to extend our comparisons by incorporating more advanced GAN architectures, such as enhanced deep super-resolution networks (EDSRs), residual channel attention networks (RCANs), and enhanced super-resolution regenerative adversarial networks (ESRGANs), which employ perceptual and adversarial losses and may further improve reconstruction quality for the GAN model.

NMC material expansion analysis

We investigated microstructural changes of NMC811 electrodes made by two different methods of DIT and dry processing over 100 cycles with high resolution and a large representative FoV. Fig. 9 illustrates the XCT images along the *x*–*y* plane of the two types of electrodes in the pristine state and after cycling. Fig. S1 in the supplementary information (SI) shows two more datasets of XCT images along the *x*–*y* plane of two other electrodes fabricated by dry processing before and after cycling to demonstrate reproducibility and provide statistics for subsequent data analysis. Fig. S2 shows the XCT images along the *x*–*z* plane (cross-section) of the four electrodes. We measured porosity and pore tortuosity in the through-electrode thickness direction (the kinetically favourable direction for ion diffusion) of each electrode in its pristine state and after 100 cycles, as summarized in Table 2. All images shown in Fig. 9, S1 and S2 are original experimental XCT scans. No deep learning-based enhancement was applied to these images.

Fig. 9, S1, S2 and Table 2 show that the DIT electrode exhibited higher porosity (0.85) and lower pore tortuosity (1.236) than the dry coated electrodes with lower porosity (0.46–0.51) and higher pore tortuosity (2.623–2.743). The lower porosity and higher tortuosity with more random microstructures of the dry coated electrodes may be caused by compression during the dry processing fabrication.[46] The NMC811 particles in the DIT electrode exhibited higher volume expansion (26%) after 100 (dis)charge cycles than 5–8% volume expansion for the dry coated electrodes. The yellow circle in Fig. 9d shows an example of a significantly expanded NMC811 particle after cycling in the DIT electrode. The yellow circle in Fig. 9b shows that while most of the NMC811 particles in the dry coated electrode expanded, the expansion rate was lower. Fig. 9b also shows crack formation between the secondary particles in the electrode (blue circle), indicating that significant strain accumulation in the more compact dry coated electrode after cycling led to microscale cracks.

To quantify the expansion of individual NMC811 particles, we plotted the particle size distributions for the four electrodes in Table 2 in their pristine state and after 100 charge–discharge cycles in Fig. S3. After 100 cycles, there was a noticeable shift in the distribution for all electrodes towards larger particle sizes, *e.g.*

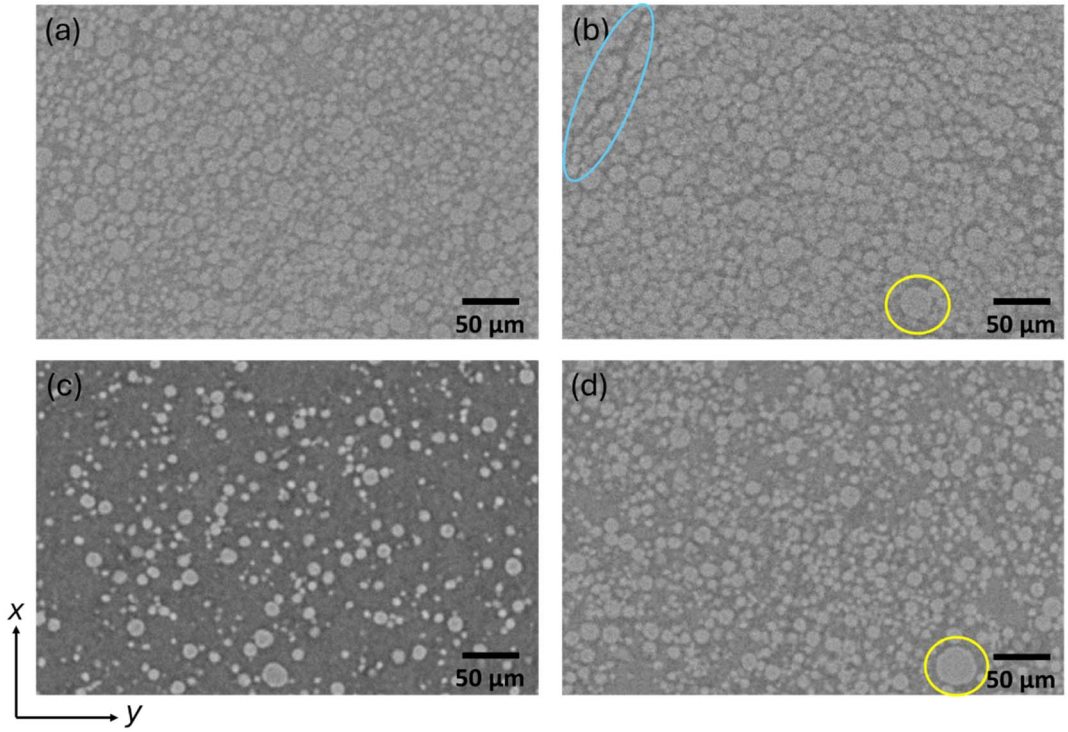

Fig. 9 XCT images along the x–y plane of the NMC811 cathodes fabricated by different methods, cycled at 0.2C. (a) Pristine dry coated electrode; (b) dry coated electrode after 100 cycles. (c) Pristine DIT electrode; (d) DIT electrode after 100 cycles. The yellow circles indicate examples of NMC811 particle expansion after 100 cycles. All these images are original experimental XCT scans and no deep learning processing was applied.

the dry coated 1 electrode showed a peak moving from 3–4 μm to 4–5 μm. Fig. 10 presents a comparative analysis of the normalized frequency distributions of pixel intensity for the XCT images of the two types of cathodes before (pristine) and after 100 cycles. In their pristine states, both types of electrodes exhibit distributions centered around lower pixel intensity values, indicating a uniform initial material structure with consistent X-ray attenuation. After 100 cycles, both types of electrodes show a shift in the pixel intensity distribution toward higher values, which are directly related to the X-ray attenuation and, consequently, suggesting an increase in the average of electrode density due to the irreversible expansion of the NMC811 particles.[47,48] The DIT electrode exhibits higher material expansion (Fig. 10b), in agreement with Table 2. In contrast, the dry electrode with lower expansion shows a lower shift. We also noticed micro-cracks appeared inside some of the secondary particles after cycling, as shown in Fig. S4. The formation of micro-cracks inside secondary particles may be due to repeated volume expansion and contraction during ion insertion and extraction particularly as NMC811 exhibits anisotropic volume expansion and shrinkage during (de)lithiation.[49]

Electrochemical performance analysis

The galvanostatic (dis)charge curves of the DIT and dry coated NMC811 cathodes (Fig. 11a) show that the dry coated cathode exhibited a slightly higher discharge capacity of 215 mA h g^{-1} in the 1st cycle compared with 202 mA h g^{-1} for the DIT cathode at 0.2C. Both capacities are comparable with the NMC811 capacities achieved by the conventional slurry coating method using the toxic NMP solvent,[50] indicating the potential for using more sustainable methods to engineer electrode microstructures. The slightly higher capacity of the dry coated electrode in the 1st cycle may be because the NMC811 particles in the pristine dry coated cathode are more connected together with higher

Table 2 Porosity and pore tortuosity of NMC811 cathodes made by DIT and dry processing methods in the pristine states and after 100 cycles at different (dis)charge rates, along with the corresponding electrode expansion after cycling

Sample	Porosity in the pristine state	Tortuosity in the pristine state	Porosity after 100 cycles	Tortuosity after 100 cycles	NMC811 particle expansion after 100 charge–discharge cycles compared to the pristine volume (%)
Dry coated 1	0.49	2.653	0.42	3.251	7
Dry coated 2	0.46	2.743	0.41	3.216	5
Dry coated 3	0.51	2.623	0.43	3.195	8
DIT	0.85	1.236	0.59	2.071	26

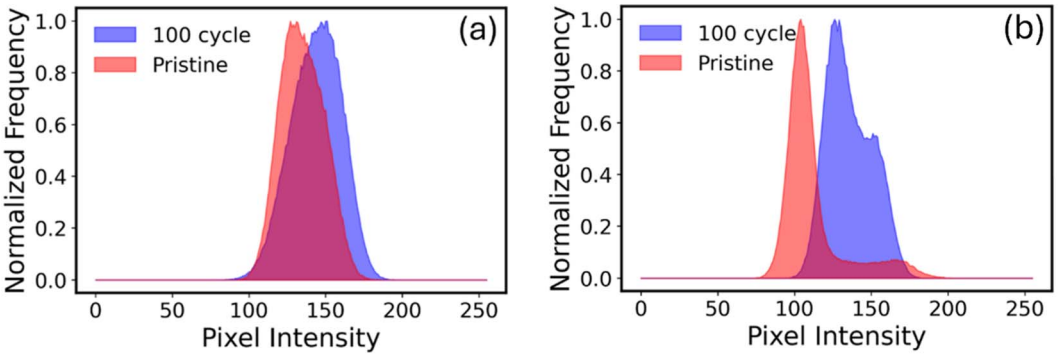

Fig. 10 Normalized frequency distribution of pixel intensity comparing the pristine state (red) and after 100 cycles (blue) for: (a) dry coated electrode; and (b) DIT electrode.

electrical conductivities where the cohesion between the NMC811 particles in the pristine DIT cathode may be lower due to higher porosity.[51] However, the discharge capacity of the dry coated cathode was reduced drastically to 64 mA h g^{-1} after 100 cycles while the discharge capacity of the DIT cathode was maintained at 148 mA h g^{-1} (more than double that of the dry coated electrode, Fig. 11b). Fig. 11b shows that both electrodes exhibited nearly 100% coulombic efficiency at the 100th cycle. The large capacity drop for the dry coated cathode is in line with the capacity decrease of other dry coated cathodes,[52] as the compression during dry electrode processing may cause microscale cracking of the NMC secondary particles that degraded performance over cycling.[51] The DIT electrode with higher porosity in the pristine state provided free space for expansion of the NMC811 individual particles over cycling and the carbon binder domain surrounding each secondary particle provided flexibility and buffered excessive strain. In contrast, the secondary particles are stacked in closer contact with each other in the low porosity dry coated electrode, causing local stress, initiating a degradation process, and leading to capacity loss over long-term cycling.

The low tortuosity of the DIT electrode improved the lithium ion diffusion kinetics and increased NMC811 active material utilization during (dis)charging, leading to larger NMC811 particle expansion.[53,54] Nevertheless, the DIT microstructure with higher porosity accommodated the larger volume expansion and strain more efficiently than the dry coated electrodes. The investigation provided valuable insights into the relationship between porosity and pore tortuosity in the pristine state and the level microstructural changes after cycling and material degradation mechanisms. The relationship among the multiple interconnected properties is challenging to be formulated by conventional methods. Hence, we performed a linear regression analysis using the porosity and tortuosity values as predictors, and the observed expansion percentages as the target variable. The fitted regression model provided the following equation for predicting material expansion:

$$\text{Expansion} = -0.0491 + (0.7286 \times \text{porosity}) + (-0.0902 \times \text{tortuosity}) \quad (1)$$

The fitted equation shows a positive relationship between porosity and expansion and a negative relationship between tortuosity and expansion. The performance of the model was evaluated by calculating MSE and the R^2 score. MSE was found to be 0.0001, and the R^2 score was 0.9982, suggesting that 99.82% of the variance in material expansion is based on

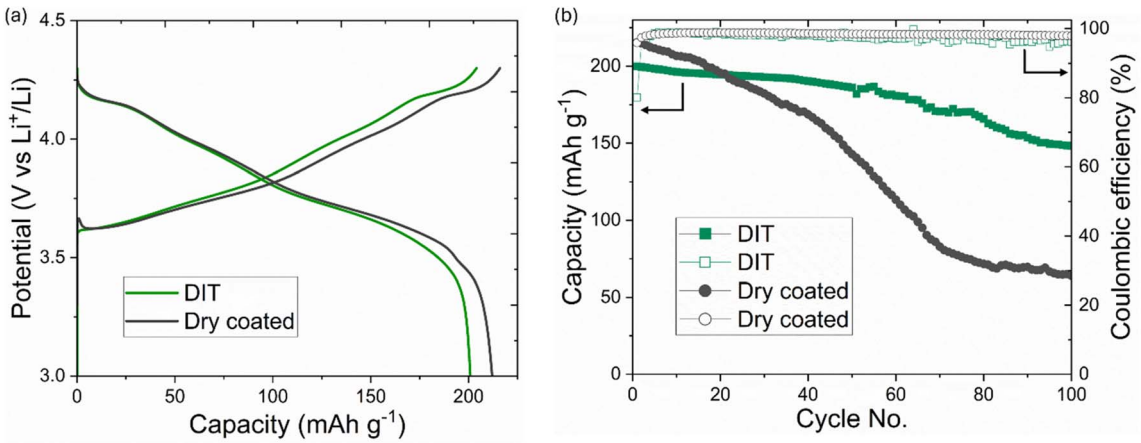

Fig. 11 (a) Galvanostatic charge and discharge curves of the 1st cycle at 0.2C; and (b) cycling stability and coulombic efficiency at 0.2C over 100 cycles; both for the NMC811 cathodes made by the DIT and dry processing methods.

porosity and tortuosity. Fig. S5 shows the fitted plate of expansion based on porosity and tortuosity.

In this study, the linear regression is presented as a descriptive observation, not predictive. The correlation among porosity and tortuosity in the pristine state and volume expansion over cycling suggest that higher porosity and lower tortuosity influence ion transport and mechanical accommodation during battery cycling. Hence, optimizing the initial electrode microstructural properties is one of the viable strategies for reducing degradation and enhancing the durability of battery electrodes.

Conclusions

This study showcases the power of integrating X-ray computed tomography (XCT) imaging with advanced deep learning models to explore the microstructural dynamics of NMC811-based cathodes during (de)lithiation cycling for lithium-ion batteries. To address the persistent challenge of the trade-off between the field of view (FoV) and resolution in imaging, we provide a framework leveraging convolutional neural networks (CNNs) and generative adversarial networks (GANs) for super-resolution enhancement of low-resolution XCT data to achieve both a large FoV and high resolution. The CNN model outperformed the GAN, achieving a structural similarity index measure (SSIM) of 0.92 *versus* 0.82 and a peak signal-to-noise ratio (PSNR) of 30.12 *versus* 26.45, enabling precise reconstruction of high-quality images with preserved fine details. Furthermore, this approach allowed us to enhance high-resolution data for larger, more representative electrodes, with a four times larger volume, offering more comprehensive visualization of active material particles and the microelectrode structure. We quantified material phase expansion ranging from 5% to 26% after 100 cycles for two different types of cathodes fabricated by different methodologies, corroborated by imaging pixel intensity shifts. The cathode fabricated by directional ice templating (DIT) that contained higher porosity and lower tortuosity in the pristine state exhibited significantly higher particle expansion after 100 cycles, indicating that the microstructure improved the ion diffusion kinetics and active material utilization, while exhibiting higher material phase expansion. Interestingly, the DIT electrode also exhibited higher capacity retention after 100 cycles compared with the electrode fabricated by dry processing with lower initial porosity and higher tortuosity. This may be because the higher initial porosity of the DIT electrode buffered the volume expansion and strain more effectively. We also developed a linear regression model to find the relationship among the interlinked properties in order to predict properties after cycling based on pristine microstructural metrics such as initial porosity and tortuosity to guide electrode microstructure design and selection of fabrication methods. This research underscores the transformative potential of combining advanced imaging with AI-driven techniques in battery research, offering deeper insights into microstructural behavior and facilitates the design of more durable and efficient energy storage solutions.

Experimental

Cathode fabrication and battery cell assembly

Cathodes in this study were fabricated by two methods, one by DIT,[13,14] and the other by dry electrode processing. For DIT, a slurry was first prepared by mixing NMC811, carbon black Super P C65, styrene-butadiene rubber (SBR) and carboxymethyl cellulose (CMC) in weight proportions of 90 : 5 : 3 : 2 in water as reported before.[55] The solid-to-solvent ratio was 40 : 60 (wt%). The mixture was homogenized using a planetary mixer at 2000 rpm for 20 minutes at room temperature (15 °C). The slurry was poured into a 3D-printed mould placed on a copper finger which was surrounded by liquid nitrogen, enabling rapid directional freezing of the slurry. The frozen cathode was immediately transferred to a freeze dryer at −40 °C and 0.1 mbar for 3 hours to completely sublime the solvent while preserving the ice-templated microstructure.[15]

For dry electrode processing, NMC811, carbon black, and polytetrafluoroethylene (PTFE) in weight proportions of 94 : 2 : 4 was first mixed using a Thinky mixer. The mixed powder was heated to 90 °C to activate the PTFE. The heated dry powder was then kneaded into a dough-like consistency; the free-standing electrodes were fabricated by applying continuous pressure, followed by laminating onto the current collectors using a hot roller at 130 °C.

For the DIT electrode (NMC811 : carbon black : styrene-butadiene rubber : carboxymethyl cellulose, 90 : 5 : 3 : 2), the thickness was 1100 μm, the areal loading was 70 mg cm^{-2}, and the density was 0.64 g cm^{-3}. For the dry electrode (NMC811 : carbon black : PTFE, 94 : 2 : 4), the thickness was 91 μm, the areal loading was 31.2 mg cm^{-2}, and the density was 3.42 g cm^{-3} , showing that the model can be applied to electrodes with a variety of properties. For both electrodes, no post-treatment calendering procedure was applied;electrochemical cycling was performed in the voltage window of 3.0–4.3 V, and the formation protocol consisted of initial activation at 0.05–0.1C for three cycles, achieving a coulombic efficiency greater than 99% and a capacity retention variation of ±4% after 100 cycles.

The electrochemical performance of the cathodes was evaluated in a half-cell configuration using CR2032 coin cells, with lithium foil serving as the counter electrode. The coin cells were assembled in an argon-filled glovebox, where H_2O and O_2 levels were controlled below 0.1 ppm to minimize contamination. The electrolyte was 1 M lithium hexafluorophosphate ($LiPF_6$) in a 1 : 1 (v/v) mixture of ethylene carbonate (EC) and ethyl methyl carbonate (EMC), and a Celgard 2400 separator was used. The configuration of the coin cells is shown in Fig. S6 in the supplementary information (SI).

X-ray computed tomography

X-ray imaging was performed using a Zeiss Versa 510 micro computed tomography scanner. All the samples used in this study were solid free-standing cathodes that were fabricated using the commercial NMC811 cathode active material, providing a representative analysis for real-world applications. The system was operated at a power of 7 W, with a source energy of 80 kV, an object magnification of 4×, an exposure time of 5

seconds, and a binning factor of 1. A photograph of the inside of the XCT scanner with the mounted sample is shown in Fig. S7. The cathodes were disassembled and cropped to a diameter of 1 mm for the low FoV experiments and 2.76 mm for the larger FoV experiments, then carefully mounted on the sample holder to ensure stability and alignment during scanning.

The resolution and FoV of the XCT images were adjusted by adjusting the distance between the sample and X-ray source. Following the completion of the scans, the acquired projection data were reconstructed. The reconstructed 3D image volumes were saved as TIFF files for analysis.

3D watershed segmentation was performed using Avizo software. For each dataset, the intensity threshold separating NMC811 particles from the background was selected adaptively to achieve the clearest phase distinction between the material phase and pore phase. The carbon binder domain (CBD) was not segmented as a separate phase because the resolution of XCT used was not able to image the CBD phase clearly and the focus of this study is on cathode active material NMC811 particles volume expansion over battery charge and discharge cycling. An example of the results of this segmentation is shown in Fig. S8. Tortuosity and porosity were quantified using image-based analysis of the segmented image using the PoreSpy library in Python. Tortuosity is defined as the ratio of the actual transport path length through the pore space to the straight-line distance, reflecting the complexity of the pore network. Porosity refers to the fraction of the volume occupied by void spaces, indicating how much of the material is porous.

Conflicts of interest

The authors declare no conflict of interest.

Data availability

The data supporting this article have been included as part of the supplementary information (SI). We will make the code used in this research publicly available on our GitHub repository. Supplementary information is available. See DOI: **https://doi.org/10.1039/d5ta05257b**.

Acknowledgements

CH acknowledges funding from the ERC Starting Grant (converted to UKRI funding EP/Y009908/1), the Faraday Institution research programme grants (FIRG060, FIRG066, FIRG082, and FIRG090), Imperial College London UKRI Impact Acceleration Account EP/X52556X/1, Imperial College London DT Prime project, and UKRI EPSRC UKRI Innovation Fellowship (EP/S001239/1 and EP/S001239/2).

References

1 M. J. B. Kabeyi and O. A. Olanrewaju, *Front. Energy Res.*, 2022, **9**, 743114.
2 K. S. Woon, Z. X. Phuang, J. Taler, P. S. Varbanov, C. T. Chong, J. J. Klemeš and C. T. Lee, *Energy*, 2023, **267**, 126502.
3 K. Shahzad and I. I. Cheema, *J. Power Sources*, 2024, **591**, 233888.
4 N. Picciano, *Battery Aging and Characterization of Nickel Metal Hydride and Lead Acid Batteries*, 2007.
5 M. Yoshio, R. J. Brodd and A. Kozawa, *Lithium-ion Batteries*, Springer, 2009.
6 A. D. A. B. A. Sofian, I. S. Imaduddin, S. Majid, T. A. Kurniawan, K. W. Chew, C.-H. Lay and P. L. Show, *J. Cleaner Prod.*, 2024, **435**, 140324.
7 G. Azimi and K. H. Chan, *Resour., Conserv. Recycl.*, 2024, **209**, 107825.
8 L. R. Brandt, J.-J. Marie, T. Moxham, D. P. Förstermann, E. Salvati, C. Besnard, C. Papadaki, Z. Wang, P. G. Bruce and A. M. Korsunsky, *Energy Environ. Sci.*, 2020, **13**(10), 3556.
9 T. Li, X.-Z. Yuan, L. Zhang, D. Song, K. Shi and C. Bock, *Electrochem. Energy Rev.*, 2020, **3**, 43.
10 C. Busà, M. Belekoukia and M. J. Loveridge, *Electrochim. Acta*, 2021, **366**, 137358.
11 S. S. Shishvan, N. A. Fleck, R. M. McMeeking and V. S. Deshpande, *J. Power Sources*, 2023, **588**, 233745.
12 A. Jangde, M. Kumar, İ. Tuğrul Gülenç, L. Wheatcroft and B. J. Inkson, *Batteries Supercaps*, 2025, e202400691.
13 C. Huang and P. S. Grant, *J. Mater. Chem. A*, 2018, **6**(30), 14689.
14 C. Huang, M. Dontigny, K. Zaghib and P. S. Grant, *J. Mater. Chem. A*, 2019, **7**(37), 21421.
15 C. Huang, C. L. A. Leung, P. Leung and P. S. Grant, *Adv. Energy Mater.*, 2021, **11**(1), 2002387.
16 K. Uzun, H. Alolaywi, S. Thapa, B. Frieberg, M. Wang, X. Huang and Y.-T. Cheng, *J. Electrochem. Soc.*, 2024, **171**(8), 080532.
17 C. Huang, M. D. Wilson, K. Suzuki, E. Liotti, T. Connolley, O. V. Magdysyuk, S. Collins, F. Van Assche, M. N. Boone and M. C. Veale, *Advanced Science*, 2022, **9**(16), 2105723.
18 C. Huang, M. D. Wilson, B. Cline, A. Sivarajah, W. Stolp, M. Boone, T. Connolley and C. L. A. Leung, *J. Phys.: Energy*, 2025, **7**, 025009.
19 M. T. Shuja, S. Thatipamula, M. W. Khan, M. Haris, R. Babarao and N. Mahmood, *Battery Energy*, 2024, **3**(2), 20230043.
20 C. Cao, M. F. Toney, T.-K. Sham, R. Harder, P. R. Shearing, X. Xiao and J. Wang, *Mater. Today*, 2020, **34**, 132.
21 C. L. A. Leung, M. D. Wilson, T. Connolley and C. Huang, *Synchrotron Radiat.*, 2024, **31**(4), 888.
22 Z. Yu, H. Shan, Y. Zhong, X. Zhang and G. Hong, *ACS Energy Lett.*, 2022, **7**(9), 3151.
23 S. Masuch, P. Gümbel, N. Kaden and K. Dröder, *Processes*, 2022, **11**(1), 10.
24 C. Huang, M. D. Wilson, B. Cline, A. Sivarajah, W. Stolp, M. N. Boone, T. Connolley and C. L. A. Leung, *Cell Rep. Phys. Sci.*, 2024, **5**(6), 101995.
25 M. J. Shojaei, B. Bijeljic, Y. Zhang and M. J. Blunt, *ACS Appl. Energy Mater.*, 2022, **5**(4), 4613.

26 M. J. Shojaei, A. Sivarajah, T. Safdar, O. V. Magdysyuke, C. L. A. Leung and C. Huang, *Solid State Ionics*, 2025, **422**, 116818.
27 R. A. Robb, E. A. Hoffman, L. J. Sinak, L. D. Harris and E. L. Ritman, *Proc. IEEE*, 1983, **71**(3), 308.
28 W. Sun and C. Huang, *J. Power Sources*, 2025, **641**, 236904.
29 C. Tian, Y. Xu, W. Zuo, B. Zhang, L. Fei and C.-W. Lin, *IEEE Trans. Multimed.*, 2020, **23**, 1489.
30 P. V. Arun, K. M. Buddhiraju, A. Porwal and J. Chanussot, *IEEE Trans. Geosci. Remote Sens.*, 2020, **58**(9), 6106.
31 Q. Lyu, C. You, H. Shan, Y. Zhang and G. Wang, *Super-resolution MRI and CT through GAN-circle, Developments in X-Ray Tomography XII*, SPIE, 2019, pp. 202–208.
32 M. Molahasani Majdabadi, Y. Choi, S. Deivalakshmi and S. Ko, *Multim. Tools Appl.*, 2022, **81**(3), 4119.
33 F. Tatsugami, T. Higaki, I. Kawashita, W. Fukumoto, Y. Nakamura, M. Matsuura, T.-C. Lee, J. Zhou, L. Cai and T. Kitagawa, *Acad. Radiol.*, 2023, **30**(11), 2497.
34 M. B. Moran, M. D. Faria, G. A. Giraldi, L. F. Bastos and A. Conci, *Comput. Biol. Med.*, 2021, **129**, 104139.
35 S. J. Jackson, Y. Niu, S. Manoorkar, P. Mostaghimi and R. T. Armstrong, *arXiv*, 2021, preprint, arXiv:2111.01270, DOI: **10.48550/arXiv.2111.01270**.
36 C. Dong, C. C. Loy, K. He and X. Tang, Learning a deep convolutional network for image super-resolution, *European Conference on Computer Vision*, Springer, 2014, pp. 184–199.
37 Y. Al Najjar, *Int. J. Sci. Res.*, 2024, **13**(3), 110.
38 M. Prodan, G. V. Vlăsceanu and C.-A. Boiangiu, *Journal of Information Systems & Operations Management*, 2023, **17**(1), 161.
39 T. Samajdar and M. I. Quraishi, Analysis and evaluation of image quality metrics, *Information Systems Design and Intelligent Applications: Proceedings of Second International Conference INDIA 2015*, Springer, 2015, vol. 2, pp. 369–378.
40 K. Szyc, An impact of different images color spaces on the efficiency of convolutional neural networks, *International Conference on Dependability and Complex Systems*, Springer, 2019, pp. 506–514.
41 J. Diaz-Cely, C. Arce-Lopera, J. C. Mena and L. Quintero, The effect of color channel representations on the transferability of convolutional neural networks, *Science and Information Conference*, Springer, 2019, pp. 27–38.
42 D. Kabakcı, *Automated Learning Rate Search Using Batch-Level Cross-Validation*, Middle East Technical University, Turkey, 2019.
43 R. Caruana, S. Lawrence and C. Giles, *Adv. Neural Inf. Process. Syst.*, 2000, **13**, 126.
44 X. Ying, *An overview of overfitting and its solutions*, Journal of physics: Conference series, IOP Publishing, 2019, p. 022022.
45 D. Saxena and J. Cao, *ACM Comput. Surv.*, 2021, **54**(3), 1.
46 W. Sun and C. Huang, *J. Power Sources*, 2024, **611**, 234774.
47 E. Laakso, S. Efimova, M. Colalongo, P. Kauranen, K. Lahtinen, E. Napolitano, V. Ruiz, J. Moškon, M. Gaberšček and J. Park, *J. Power Sources*, 2024, **599**, 234159.
48 B. L. Rinkel, J. P. Vivek, N. Garcia-Araez and C. P. Grey, *Energy Environ. Sci.*, 2022, **15**(8), 3416.
49 H. Pegel, O. von Kessel, P. Heugel, T. Deich, J. Tübke, K. P. Birke and D. U. Sauer, *J. Power Sources*, 2022, **537**, 231443.
50 G. J. P. Fajardo, M. Belekoukia, S. Bolloju, E. Fiamegkou, A. S. Menon, Z. Ruff, Z. Shen, N. Shah, E. Björklund and M. J. Zuba, *RSC Appl. Interfaces*, 2024, **1**(1), 133.
51 W. M. Dose, J. K. Morzy, A. Mahadevegowda, C. Ducati, C. P. Grey and M. F. De Volder, *J. Mater. Chem. A*, 2021, **9**(41), 23582.
52 R. C. McNulty, E. Hampson, L. N. Cutler, C. P. Grey, W. M. Dose and L. R. Johnson, *J. Mater. Chem. A*, 2023, **11**(34), 18302.
53 C. Huang, N. P. Young, J. Zhang, H. J. Snaith and P. S. Grant, *Nano energy*, 2017, **31**, 377.
54 C. Huang, J. Zhang, N. P. Young, H. J. Snaith and P. S. Grant, *Sci. Rep.*, 2016, **6**(1), 25684.
55 G. Li, J. Su and C. Huang, *Small Sci.*, 2025, 2500198.